

Two Real Scalar WIMP Model in the Assisted Freeze-Out Scenario

Bastián Díaz Sáez^{*1}, Kilian Möhling^{†2}, and Dominik Stöckinger^{‡2}

¹*Physik-Department, Technische Universität München, James-Franck-Straße, 85748 Garching, Germany*

²*Institut für Kern- und Teilchenphysik, TU Dresden, Zellescher Weg 19, 01069 Dresden, Germany*

Abstract

We study a simple dark matter model given by two interacting real singlet scalars, with only one of them coupled to the Higgs. The model therefore presents a minimal *assisted-freeze-out* framework: both scalars contribute to the dark matter relic density, but only one of them takes part in the elastic scattering with nuclei. This reduces the expected interaction rate in direct detection experiments in such a way that the model in some regions of the parameter space may evade XENON1T constraints. We explore the model under theoretical (perturbativity, stability potential and unitarity) and experimental constraints (Higgs to invisible, relic density, direct detection), with the use of the narrow-width-approximation near the Higgs resonance to calculate the averaged annihilation cross section. We show that the model is viable in the Higgs resonance region and for scalar singlets masses of hundreds of GeV, although the model becomes highly constrained at high energies.

*bastian.diaz@tum.de

†kilian.moehling@tu-dresden.de

‡dominik.stoeckinger@tu-dresden.de

Contents

1	Introduction	2
2	Model and Theoretical Constraints	4
3	Relic Abundance	6
3.1	Boltzmann equations	6
3.2	Assisted freeze-out	8
4	Dark Matter Phenomenology	10
4.1	Experimental Constraints	10
4.2	Scan Results	11
4.3	Landau Poles	14
5	Discussion and Summary	16
6	Acknowledgment	17
A	Average Annihilation Cross Sections	17
B	$S_2 S_2 h$ vertex at one-loop	18

1 Introduction

While cosmological observations over the past years have made it more and more apparent that Dark Matter (DM) is an important part of our universe [1], direct detection experiments have put strong constraints on the parameter space of many WIMP models, in particular one of the most popular DM models: the real singlet scalar or also called *Singlet Higgs Portal* (SHP) [2, 3]. Even when considering the singlet scalar as just a partial DM source together with additional non-thermal contributions (e.g. axions [4]), most of the parameter space around a few hundred GeV up to the TeV scale is ruled-out. Following this minimal approach, models with two real singlet scalars have been studied in the last years, reopening the possibility of having scalar DM near the weak scale. Two classes of models have been explored: one scalar stabilized by a Z_2 symmetry with the other scalar being unstable [5, 6, 7, 8, 9, 10, 11, 12] or both scalars stabilized by two symmetries $Z_2 \times Z'_2$ [11, 13, 14, 15, 16, 17, 18, 19]¹. In the latter case, when the two scalars are WIMPS with sizable interaction between them [17], the model may give the correct relic density on large portions of the parameter space, but most of it is excluded by XENON1T direct detection results. Only the Higgs resonance region, where a more careful treatment of the thermally averaged annihilation cross section is necessary, seems

¹Fermions and vectors have also been considered in similar frameworks, e.g. [20, 21, 22].

to remain viable. In view of this, it may be of interest to look for regions of parameter space in this framework which evade the strong direct detection constraints, possibly allowing DM with masses of several hundred GeV up to a few TeV. For instance, in [11] (also see [23, 24]) such a two-component scalar model is explored under the assumption that one of the scalars couples very weakly to the Higgs ($\lambda \sim 10^{-5}$), giving rise to a chronology in the decoupling process (*exchange driven freeze-out*), with DM conversion being a pivotal process in the determination of the relic abundance. They show that this mechanism successfully evades XENON1T bounds, allowing DM with masses of hundreds of GeV, provided certain quartic coupling take values above the unity.

In this work we study the two real scalar model, both stable gauge singlets, with one of the Higgs portals set to zero. In this regime the model becomes a minimal realization of an appealing idea, the so-called assisted freeze-out mechanism [13] (for a previous similar idea see [25]). The motivation of this approach is that only one of the scalars interacts directly with baryonic matter through its Higgs portal, whereas the other scalar may contribute most to the DM budget. In this way, the Higgs coupled scalar may evade the direct detection constraints more easily due to the rescaling of the expected DM direct detection rate by its partial abundance: $\Omega_{coupled}/\Omega_{total}$. Qualitatively, this framework can be viewed as an approximation of the exchange driven freeze-out [11].

We study the parameter space in detail to identify viable coupling and mass ranges of the assisted freeze-out framework. For masses above the Higgs resonance, we find that large couplings $\lambda \gtrsim 1$ are required in order to pass both direct detection and relic density constraints, in agreement with [11]. We then further impose theoretical constraints on the resulting parameter space in order to see to what extent the resulting high couplings are consistent with perturbative, scalar potential stability and unitarity constraints. We also specifically study the resonance effects for DM masses around 60 GeV, half of the Higgs boson mass, where the real singlet scalar in SHP is not yet ruled out. Finally, we study the effects of the renormalization group equations on the remaining parameter space after applying theoretical and experimental constraints.

In the following section, we present the model along with the theoretical constraints. In section 3, we present the corresponding Boltzmann equations, approximations to the averaged annihilation cross section and we study the predicted relic abundance in detail, specifically in comparison with the SHP. In section 4, we show some scan results inside and outside the resonance region, taking into account the various constraints including those given by Landau poles of the model. Finally, we give a brief summary and the conclusions in section 5.

2 Model and Theoretical Constraints

The model introduces two real gauge singlet scalars S_1 and S_2 , each one stabilized by $\mathbb{Z}_2 \times \mathbb{Z}'_2$ symmetry, with the fields transforming as:

$$\mathbb{Z}_2: S_1 \rightarrow -S_1, S_2 \rightarrow S_2, \text{SM} \rightarrow \text{SM}, \quad (1a)$$

$$\mathbb{Z}'_2: S_1 \rightarrow S_1, S_2 \rightarrow -S_2, \text{SM} \rightarrow \text{SM}. \quad (1b)$$

Consequently, the scalar potential for this model is

$$V(H, S_1, S_2) = \mu_H^2 |H|^2 + \lambda_H |H|^4 + \sum_{i=1,2} \left(\frac{\mu_i^2}{2} S_i^2 + \frac{\lambda_i}{4!} S_i^4 + \frac{\lambda_{Hi}}{2} |H|^2 S_i^2 \right) + \frac{\lambda_{12}}{4} S_1^2 S_2^2. \quad (2)$$

The tree-level scalar masses after EWSB are

$$m_h^2 = 2v_H^2 \lambda_H, \quad (3)$$

$$m_i^2 = \mu_i^2 + \frac{1}{2} v_H^2 \lambda_{Hi}, \quad (4)$$

with v_H the Higgs vacuum expectation value of 246 GeV. In order for the singlet scalars to not acquire a vacuum expectation value, we set $\mu_i^2 > 0$, then the physical scalar states are: $\{h, S_1, S_2\}$.

According to the normalization of our scalar potential eq. (2), the stability of the potential at tree-level requires [26, 27, 28]

$$\lambda_H > 0, \quad \lambda_1 > 0, \quad \lambda_2 > 0, \quad \lambda_a > 0, \quad \lambda_b > 0, \quad \lambda_c > 0, \quad (5)$$

$$\sqrt{2\lambda_H \lambda_1 \lambda_2 / 9} + \lambda_{H1} \sqrt{\lambda_2 / 3} + \lambda_{H2} \sqrt{\lambda_1 / 3} + \sqrt{2\lambda_a \lambda_b \lambda_c} > 0, \quad (6)$$

where $\lambda_a \equiv \lambda_{H1} + \sqrt{2\lambda_H \lambda_1 / 3}$, $\lambda_b \equiv \lambda_{H2} + \sqrt{2\lambda_H \lambda_2 / 3}$ and $\lambda_c \equiv \lambda_{12} + \sqrt{\lambda_1 \lambda_2 / 9}$. Taking $m_h = 125$ GeV in eq. (3) gives $\lambda_H = 0.13$.

On the other hand, tree-level perturbative unitarity puts constraints on the zeroth partial wave of the system [29, 30], which for a $2 \rightarrow 2$ elastic scattering is given by

$$a_0 = \frac{1}{32\pi} \sqrt{\frac{4|\vec{p}_f| |\vec{p}_i|}{s}} \int_{-1}^{+1} \mathcal{M}_{2 \rightarrow 2} d \cos \theta, \quad (7)$$

with s the center-of-mass frame (CM) energy and $p_{i,f}^{\text{CM}}$ the tree-momenta of initial and final particles in the CM. Unitarity then requires $|\text{Re}(a_0)| \leq \frac{1}{2}$. Considering the six-channel system

$$\{hh, S_1 S_1, S_2 S_2, S_1 S_2, h S_1, h S_2\}, \quad (8)$$

²From these last constraints we obtain that, for instance, if λ_{H1} is negative, it must to satisfy $\lambda_{H1}^2 < 2\lambda_H \lambda_2 / 3$, and if it is positive, then $\lambda_{H1} > 0$.

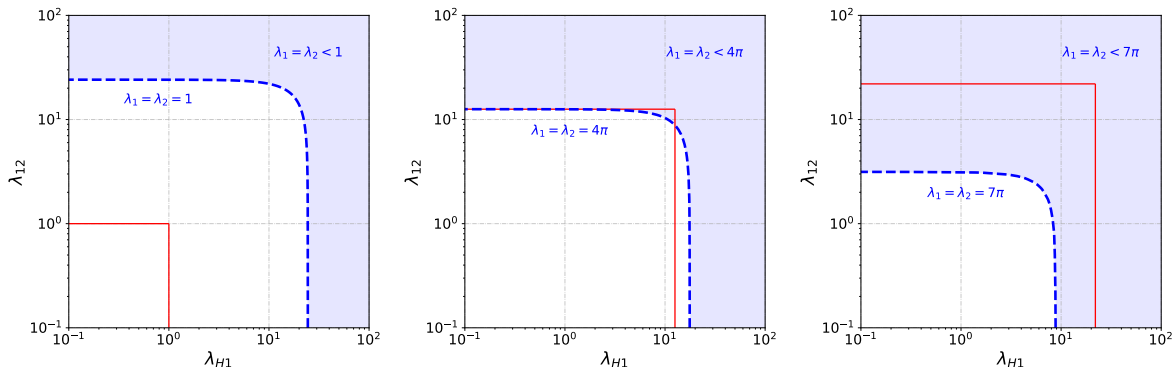


Figure 1: Unitarity constraints on the pair $(\lambda_{H1}, \lambda_{12})$ for $\lambda_{1,2} = 1, 4\pi, 7\pi$, respectively, with the blue region excluded by this constraint. The region inside of each red square may be interpreted as the allowed parameter space by perturbativity when the perturbative limit on the couplings is $1, 4\pi, 7\pi$, respectively.

the zero-partial wave matrix at high energies $s \gg m_h, m_1, m_2$ is

$$a_0 \rightarrow \frac{1}{16\pi} \begin{pmatrix} 3\lambda_H & \lambda_{H1} & \lambda_{H2} & 0 & 0 & 0 \\ \lambda_{H1} & \lambda_1 & \lambda_{12} & 0 & 0 & 0 \\ \lambda_{H2} & \lambda_{12} & \lambda_2 & 0 & 0 & 0 \\ 0 & 0 & 0 & \lambda_{12} & 0 & 0 \\ 0 & 0 & 0 & 0 & \lambda_{H1} & 0 \\ 0 & 0 & 0 & 0 & 0 & \lambda_{H2} \end{pmatrix}. \quad (9)$$

Perturbative unitarity constraints on the matrix a_0 result in bounds on its eigenvalues e_i . In this work we concentrate on the case in which $\lambda_{H2} = 0$, which then results in the following constraint on the eigenvalues of the 3×3 upper block

$$|e_i(\lambda_1, \lambda_2, \lambda_{H1}, \lambda_{12})| \leq 8\pi, \quad i = 1, 2, 3. \quad (10)$$

For simplicity we omit the analytical expressions for each eigenvalue.

Another theoretical constraint is given by perturbativity, which implies approximate upper limits for all coupling in order the perturbative expansion be reliable. At this point we do not choose any specific value for these upper limit. In the following discussions we take into account all three theoretical constraints (stability, unitarity and perturbativity) and analyze their impact on the viable parameter space.

Considering only positive values for λ_{H1} and λ_{12} (negative values do not change the analysis of our work) then the stability potential constraints eq. (5) do not give any new information. In Fig. 1 we show the unitarity bounds on λ_{H1} and λ_{12} for the choices $\lambda_{1,2} = 1, 4\pi$ and 7π , respectively, with the blue region excluded by this constraint. The bigger the values of the quartic couplings $\lambda_{1,2}$ the stronger are the constraints on the remaining pair $\lambda_{H1}, \lambda_{12}$. In

particular, as the middle plot shows, it is not possible to have the quartic couplings $\lambda_{1,2}$ and $\lambda_{H1}, \lambda_{12}$ all simultaneously with values above 4π . Additionally, the region inside the red squares indicates the regions allowed by different choices of the perturbativity limit. The limits are set to 1, 4π , and 7π , respectively, i.e. to the same values as the quartic couplings in each plot. Clearly, perturbativity places limits on each individual coupling, while unitarity places limits on combinations of couplings. If very strong perturbativity limits are imposed as in the left plot, unitarity does not imply additional constraints, while very loose perturbativity limits, as in the right panel, are much less stringent than unitarity limits.

Therefore, the analysis shows that the theoretical constraints depend on both the assumed values for the quartic couplings $\lambda_{1,2}$ as well as the choice of the perturbativity limit. In the last part of this work, when we contrast theoretical and experimental constraints on the model, we discuss the viability of parameter space depending on the chosen criteria.

3 Relic Abundance

In this section we discuss the main formulas describing the evolutions of the DM number density throughout the thermal history. We introduce precise approximations for the averaged annihilation cross section and study the behavior of the DM relic density both in and outside the Higgs resonance region. We also point out that a careful treatment of the averaged annihilation cross section near the Higgs resonance is necessary in order to obtain the correct results.

3.1 Boltzmann equations

The coupled Boltzmann equations for the DM number densities of S_1 and S_2 are given by

$$\begin{aligned} \frac{dn_1}{dt} + 3Hn_1 &= - \langle \sigma_{11XX} v \rangle \left[n_1^2 - n_{1e}^2 \right] - \langle \sigma_{1122} v \rangle \left[n_1^2 - \frac{n_{1e}^2}{n_{2e}^2} n_2^2 \right] \Theta(m_1 - m_2) \\ &\quad + \langle \sigma_{2211} v \rangle \left[n_2^2 - \frac{n_{2e}^2}{n_{1e}^2} n_1^2 \right] \Theta(m_2 - m_1), \\ \frac{dn_2}{dt} + 3Hn_2 &= - \langle \sigma_{22XX} v \rangle \left[n_2^2 - n_{2e}^2 \right] - \langle \sigma_{2211} v \rangle \left[n_2^2 - \frac{n_{2e}^2}{n_{1e}^2} n_1^2 \right] \Theta(m_2 - m_1) \\ &\quad + \langle \sigma_{1122} v \rangle \left[n_1^2 - \frac{n_{1e}^2}{n_{2e}^2} n_2^2 \right] \Theta(m_1 - m_2), \end{aligned} \tag{11}$$

with X being some SM particle, $\langle \sigma v \rangle$ the thermal average of the cross section times the relative velocity of a given process $ii \rightarrow jj$, with $i, j = 1, 2, X$, and, assuming a Maxwell-Boltzmann thermal distribution, the equilibrium number densities n_{ie} as a function of the thermal bath temperature T are given by

$$n_{ie}(T) = g_i \frac{m_i^2}{2\pi^2} T K_2\left(\frac{m_i}{T}\right), \tag{12}$$

with the internal degrees of freedom g_i , and the modified Bessel function of the second kind K_2 . Furthermore, the Hubble parameter H and entropy density s in the early universe can be written as

$$H(T) = \sqrt{\frac{4\pi^3 G}{45} g_*(T)} \cdot T^2, \quad s(T) = \frac{2\pi^2}{45} g_{*s}(T) \cdot T^3, \quad (13)$$

with G is the Newton gravitational constant, and $g_*(T)$ and $g_{*s}(T)$ are the effective degrees of freedom contributing respectively to the energy and the entropy density at temperature T . For our numerical evaluations we interpolate g_* and g_{*s} from the values given in [31]. We have introduced Heaviside functions in eq. (11) in order to select the formulation of the interaction term in which $n_{ie}^2/n_{je}^2 \rightarrow 0$ at small T , making the numerical evaluation more convenient.

Lastly, introducing $x := \mu/T$, where $\mu = m_1 m_2 / (m_1 + m_2)$ and $Y_i := n_i/s$, we rewrite eq. (11) in the usual dimensionless form

$$\begin{aligned} \frac{dY_1}{dx} &= -\lambda_{11XX} \cdot [Y_1^2 - Y_{1e}^2] - \lambda_{1122} \cdot [Y_1^2 - r_{12}^2 Y_2^2] \cdot \Theta(m_1 - m_2) \\ &\quad + \lambda_{2211} \cdot [Y_2^2 - r_{21}^2 Y_1^2] \cdot \Theta(m_2 - m_1), \\ \frac{dY_2}{dx} &= -\lambda_{22XX} \cdot [Y_2^2 - Y_{2e}^2] - \lambda_{2211} \cdot [Y_2^2 - r_{21}^2 Y_1^2] \cdot \Theta(m_2 - m_1) \\ &\quad + \lambda_{1122} \cdot [Y_1^2 - r_{12}^2 Y_2^2] \cdot \Theta(m_1 - m_2), \end{aligned} \quad (14)$$

with

$$r_{ij}(x) := \frac{Y_{ie}(x)}{Y_{je}(x)}, \quad \lambda_{ijjj}(x) := \frac{\langle \sigma_{ijjj} v \rangle(x) \cdot s(T)}{x \cdot H(T)} \quad \text{for } i, j = 1, 2, X. \quad (15)$$

The thermal average annihilation cross section is given by

$$\langle \sigma_{ijjj} v \rangle(x) = \int_{4m_i^2}^{\infty} \frac{s \sqrt{s - 4m_i^2} K_1(\sqrt{s} \frac{x}{\mu}) (\sigma v)_{ijjj}}{16 \frac{\mu}{x} m_i^4 K_2^2(m_i \frac{x}{\mu})} ds, \quad (16)$$

where K_1 and K_2 are modified Bessel functions of the second kind. Properly evaluating this expression plays a significant role in determining the DM relic density, especially near resonances and thresholds³. In order to evaluate eq. (16), we use the narrow width approximation (NWA) in the resonance region [33, 34], whereas outside of it we took the constant approximation $\langle \sigma v \rangle = \sigma v (s = 4m_i^2)$. We used the perturbative tree-level σv into kinematically open channels, with the total decay width of the Higgs boson $\Gamma_h = 1.34 \times 10^{-3}$ MeV, supplemented with the invisible decay width when $m_1 \leq m_h/2$. These cross sections are in agreement with the analytic

³The expression (16) is based on the assumption of local thermal equilibrium when chemical decoupling is taking place. However, near a resonance, this assumption may be no longer valid, then a more involved treatment must to be carried [32]. We will comment more about this point in Sec. 4.2.

results obtained in [17]. We solved the Boltzmann equations in eq. (14) numerically using *solve-ivp* from Scipy module in Python. Our results have been cross-checked with MicrOMEGAS.

Finally, after solving the Boltzmann equations the DM density parameter is given by

$$\Omega h^2 = \Omega_1 h^2 + \Omega_2 h^2, \quad \Omega_i h^2 = \frac{2.9713 \cdot 10^9}{10.5115 \text{ GeV}} \cdot Y_{i,0} \cdot m_i, \quad (17)$$

where $Y_{i,0}$ is the yield of S_i today, i.e. after freeze-out.

3.2 Assisted freeze-out

We now focus on the assisted freeze-out scenario, i.e. we set one Higgs portal coupling to zero, $\lambda_{H2} = 0^4$. In this way, from now on only S_1 will be *coupled* to the SM, whereas S_2 becomes *decoupled*. Consequently, $\lambda_{22XX} = 0$ in eq. (14) and the relevant parameters of this scenario are m_1, m_2, λ_{H1} and λ_{12} . We allow sizable couplings λ_{H1} and λ_{12} , such that the coupled scalar starts in thermal equilibrium with the SM, and at the same time brings the decoupled one into the equilibrium too. In the second part of this section we exemplify the assisted freeze-out mechanism, showing clear differences between the predictions of the real singlet scalar S in the *Singlet Higgs Portal* model (SHP) [2] and the equivalent S_1 scalar in this scenario.

The dynamics of the abundance evolution is highly dependent on the mass hierarchy of the two singlet scalars. The behaviour of the resulting relic densities can be seen in more detail in Fig. 2 (left), which fixes $m_1 = 100$ GeV and varies m_2 . For $m_2 < m_1$ (inverted hierarchy) the overwhelmingly dominant contribution to the total relic comes from Ω_2 , while in the normal mass hierarchy ($m_2 > m_1$) $\Omega \approx \Omega_2$ only at very high mass differences with a much smaller relative difference between Ω_1 and Ω_2 . Again, this behaviour can be understood by looking at the corresponding Boltzmann Equation. In the normal hierarchy we already mentioned that if $m_2 \gg m_1$, we expect Y_2 to evolve independently of Y_1 . In fact, since $\langle \sigma_{2211} v \rangle \sim m_2^{-2}$, eq. (14) effectively decouples, resulting in $Y_1 \sim \text{const.}$ (i.e. $\Omega_1 \sim \text{const.}$) and $Y_2 \sim m_2^2$ ($\Omega_2 \sim m_2^3$), as it is shown in Fig. 2 (left) with the blue and red lines, respectively. Although in the normal hierarchy at high mass differences we have $\Omega_2 \gg \Omega_1$, we typically obtain a too small overall DM relic abundance. This suggests that we would have to go to smaller couplings λ_{H1} , which in turn will produce larger relative contribution of Ω_1 to Ω . In the inverted hierarchy, constraints on the DM relic abundance also put very strong constraints on the possible masses m_2 for given m_1, λ_{H1} and λ_{12} . This will be an important point to keep in mind when choosing the mass resolution in parameter space scans.

Considering the λ_{12} dependence of the DM relic abundance, we would expect a larger coupling to lead to a later freeze out and therefore lower relic densities. For small couplings

⁴In Appx. B we discuss about the effects of radiative corrections of the renormalized value of λ_{H2} on the relic abundance calculation. The effects of radiative λ_{H2} becomes non-negligible only in those cases in which the combination $\lambda_{H1}\lambda_{12}$ takes very high values, then in this way deviating the predictions of the relic density values found in the rest of the paper (i.e. $\lambda_{H2} = 0$) at most in a factor of two. For studies considering a non-vanishing tree-level value λ_{H2} see [17].

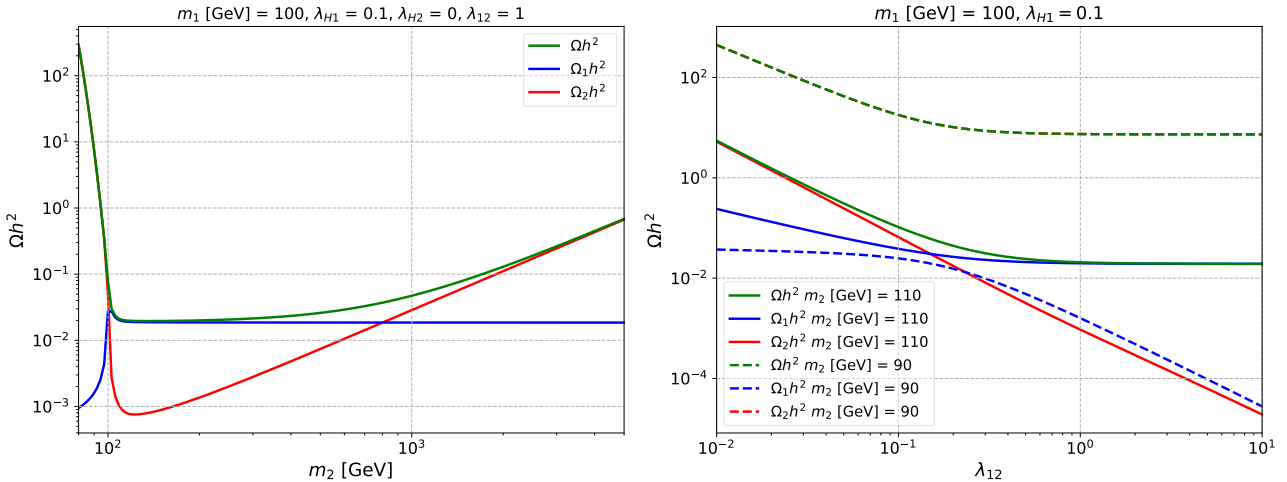


Figure 2: DM density parameters Ωh^2 (green), $\Omega_1 h^2$ (blue) and $\Omega_2 h^2$ (red) as functions of m_2 (left) and λ_{12} (right), with $m_1 = 100$ GeV and $\lambda_{H1} = 0.1$ in both plots. In the left plot we have set $\lambda_{12} = 1$, and in the right plot $m_2 = 90$ GeV (dashed) and $m_2 = 110$ GeV (solid).

$\lambda_{12} \sim \lambda_{H1}$ this behavior can indeed be seen in Fig. 2 (right), however, at large couplings $\lambda_{12} \gg \lambda_{H1}$, Ω becomes asymptotically constant. In the normal mass hierarchy this is again explained by the fact that $dY_2/dx \sim -\lambda_{2211}Y_2^2$, and therefore $Y_2 \sim 1/\lambda_{12}^2$. Since the interaction term is subsequently roughly proportional to $\lambda_{12}^2 Y_2^2 \sim 1/\lambda_{12}^2$, we find $Y_1 \sim const.$ at large couplings. Interestingly, in the inverted mass hierarchy the total relic abundance behaves very much in the same way, although the independence of Ω on λ_{12} at large couplings now comes from the fact that $Y_2 \sim const.$ The explanation is very similar to that in the normal hierarchy: we have $dY_1/dx \sim -\lambda_{1122}Y_1^2$, i.e. $Y_1 \sim 1/\lambda_{12}^2$ and therefore $Y_2 \sim const.$

Having made a detailed analysis of the relic abundances as a function of the parameters, here we exemplify the mechanism operating in the inverted hierarchy that will be useful in the rest of the paper. In Fig. 3 we show the evolution of Y_1 (solid blue line) and Y_2 (solid red line) as a function of x when the assisted mechanism is present, with the dashed blue and red lines corresponding to the equilibrium densities of S_1 and S_2 , respectively. Right after S_1 decouples from the SM thermal bath, it enters into a new equilibrium y_{1e} (green dashed line), where annihilations $S_1 S_1 \rightarrow S_2 S_2$ continue being effective, decreasing Y_1 much more than in the singlet scalar in the Singlet Higgs Portal (SHP) (grey solid curve). The modified equilibrium function is given by $\langle \sigma_{1122} v \rangle (Y_{1e}/Y_{2e})^2 Y_2^2$, obtained directly from the Boltzmann equation in eq. (14). This behavior is a generic feature of interacting multicomponent DM [21, 17], which we will utilize to evade direct detection constraints. Finally, this effect is present independent of the value of m_1 , but it depends strongly on the singlet mass difference and λ_{12} , as exemplified in Fig. 2.

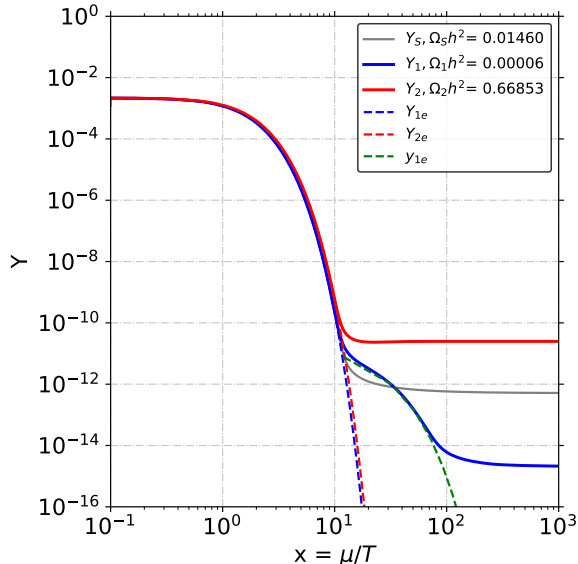


Figure 3: Thermal evolution of the abundances in the assisted freeze-out scenario as a function of x , for $m_1 = 100$ GeV, $m_2 = 95$ GeV and $(\lambda_{H1}, \lambda_{H2}, \lambda_{12}) = (0.1, 0, 10)$. The blue (red) solid line corresponds to yield of S_1 (S_2), and the gray one the yield of the singlet scalar in the SHP. The dashed blue and red lines correspond to the equilibrium densities of S_1 and S_2 , respectively, whereas the green dashed line corresponds to the new equilibrium y_{1e} that S_1 follows after it decouples from the SM bath.

4 Dark Matter Phenomenology

In this section, we start reviewing relevant experimental constraints, such as Higgs decay to invisible at the LHC, relic density and direct detection, to subsequently applied them onto the promising parameter space of the model. Similarly to the last section, we focus on the Higgs resonance region separately and contrast the results with the SHP predictions. Finally, we present some scans on the parameter space outside the Higgs resonance, contrasting those points that fulfill the experimental constraints with theoretical bounds.

4.1 Experimental Constraints

The strongest constraint on the parameter space is given by the observed DM relic abundance. We use the value given by the most recent Planck data [1]:

$$\Omega_c h^2 = 0.11933 \pm 0.00091, \quad \text{at } 2\sigma. \quad (18)$$

We will denote this measured value of the DM relic by Ω_c and the DM relic predicted by the model by Ω . This gives a parameter space constraint $\Omega = \Omega_c$, which we applied with a tolerance of $\pm 5\%$ accounting for uncertainties in our computation.

The second constraint we need to pass is given by direct detection experiments such as XENON1T. These give an upper bound on the spin-independent (SI) DM nucleon scattering cross section σ_{SI} ,

$$\sigma_{SI,i} = \frac{\lambda_{Hi}^2 f_N^2}{4\pi} \frac{\mu_i^2 m_n^2}{m_h^4 m_i^2}, \quad i = 1, 2, \quad (19)$$

with $f_N = 0.3$ the effective Higgs-nucleon coupling, $m_n = 0.9$ GeV the nucleon mass and $\mu_i = m_n m_i / (m_n + m_i)$ the DM-nucleon reduced mass [2, 3]. Since in our case only one of the scalars interacts with the SM, i.e. S_1 , the differential detection rate is $dR/dE \propto \sigma_{SI} n_{1\odot} = \sigma_{SI} (\Omega_1/\Omega) n_{\odot}$, where n_{\odot} denotes the local DM density. This effectively rescales the direct detection constraint on our model to $(\Omega_1/\Omega) \sigma_{SI,1} \leq \sigma_{Xe}$, where σ_{Xe} is the upper bound given by XENON1T [35]. In the SHP, it has been shown that indirect bounds set much weaker constraints on the parameter space than the direct detection limits [2]. In our scenario, this still holds, since the only parameter space passing the stringent XENON1T constraints is in the inverted mass hierarchy where $\Omega_1/\Omega \ll 1$, therefore primary fluxes produced from the annihilation of a pair of S_1 are highly suppressed.

Lastly, for $m_1 \leq m_h/2$, the Higgs boson can decay into two S_1 , with an invisible decay width given by

$$\Gamma_{inv}(h \rightarrow S_1 S_1) = \frac{\lambda_{H1}^2 v_H^2}{32\pi m_h} \sqrt{1 - \frac{4m_1^2}{m_h^2}}. \quad (20)$$

This contributes to the invisible branching rate $\text{Br}(h \rightarrow \text{inv}) = \Gamma_{inv}/(\Gamma_{\text{SM}} + \Gamma_{inv})$, with $\Gamma_{\text{SM}} = 4.07$ MeV [36]. Experimental searches put strong constraints on this quantity, with the most stringent value being given by $\text{Br}(h \rightarrow \text{inv}) < 0.19$ at 95% C.L. [36].

4.2 Scan Results

In Fig. 4 we show some numerical values in the resonance region to exemplify the general behavior here. In this plot, we have considered contours with fixed mass differences $m_2 = m_1 + 1$ GeV (blue), $m_1 - 1$ GeV (green) and $m_1 - 5$ GeV (grey), which give the observed DM relic abundance at $\lambda_{12} = 1$. As expected, in the normal mass hierarchy S_1 behaves very similar to S , however in the inverted hierarchy, Ω_1 drops enough such that direct detection constraint becomes effectively negligible, only ruling out parameter space outside the Higgs resonance region ⁵. For comparison, we have also plotted contours where the SHP could account for the

⁵As we pointed out in a footnote in page 7, near the resonance kinetic equilibrium can be lost, requiring a more precise treatment to obtain the correct relic abundance in this region. In our case, where only S_1 couples

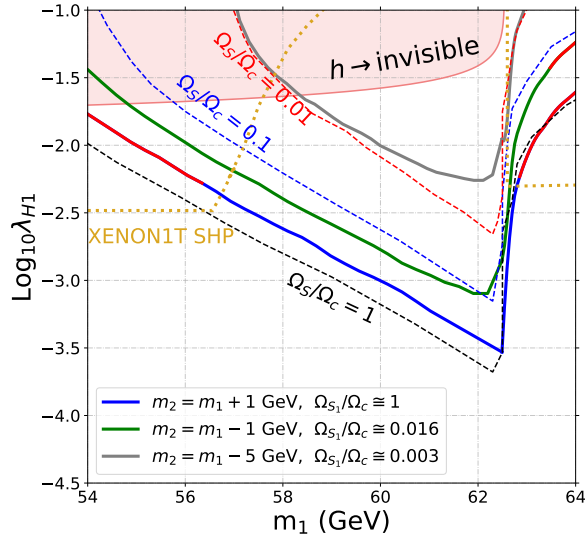


Figure 4: Contours of fixed relic abundance in the assisted freeze-out model (solid) and in the SHP (dashed) in the parameter space (m_1, λ_{H1}) around the Higgs resonance. All contours of the assisted freeze-out model fulfill $\Omega = \Omega_c$ with $\lambda_{12} = 1$, for different mass splittings $m_2 - m_1$. The light red region is ruled out due to the Higgs to invisible constraint, and the region above the gold contour is ruled out in the SHP by the XENON1T data. The red solid lines denote the regions ruled out by the direct detection constraints on the assisted freeze out model.

100%, 10% and 1% of the correct relic abundance with a black, blue and red dashed lines, respectively. As expected, due to the additional degrees of freedom coming from m_2 and λ_{12} , the two scalar model can explain the entire DM relic abundance in that region but also even at slightly smaller masses m_1 . Thus, for masses near the Higgs resonance the SHP parameter space opens up in the two scalar model and it remains to be seen, whether WIMPs in the region can be fully ruled out as DM candidates.

Outside the Higgs resonance region, the most promising parameter space is in the inverted mass hierarchy ($m_2 < m_1$), as by our analysis from section 3.2, both the abundance and direct detection constraints are most easily fulfilled there. We thus ran larger scans of points $(m_2, \lambda_{H1}, \lambda_{12})$ for fixed $m_1 = 100$ GeV (Fig. 5) and $m_2 < m_1$. Precisely, the parameter space is sampled using equal spacing for $\lambda_{12} \in (1, 10)$ and $m_2 \in (80, 100)$ and logarithmic spacing for $\lambda_{H1} \in (0.01, 1)$ with a total number of points $n = 18000$. The grid scan used equal spacing with 50 steps for $m_2 \in (90, 100)/(470, 500)$ and 20 steps for $\lambda_{H1} \in (0.05, 0.6)/(0.3, 2.5)$ and $\lambda_{12} \in (5, 15)$. In this region, points fulfilling the direct detection constraints (red) are either

to the Higgs, this effect should be more prominent when Ω_1 is dominant (normal hierarchy), with expected changes equivalent to those obtained in [32] for the SHP. In the inverse hierarchy, where Ω_1 is sub-dominant, we expect a small correction to the total relic abundance. We did not consider such a precise treatment in this work.

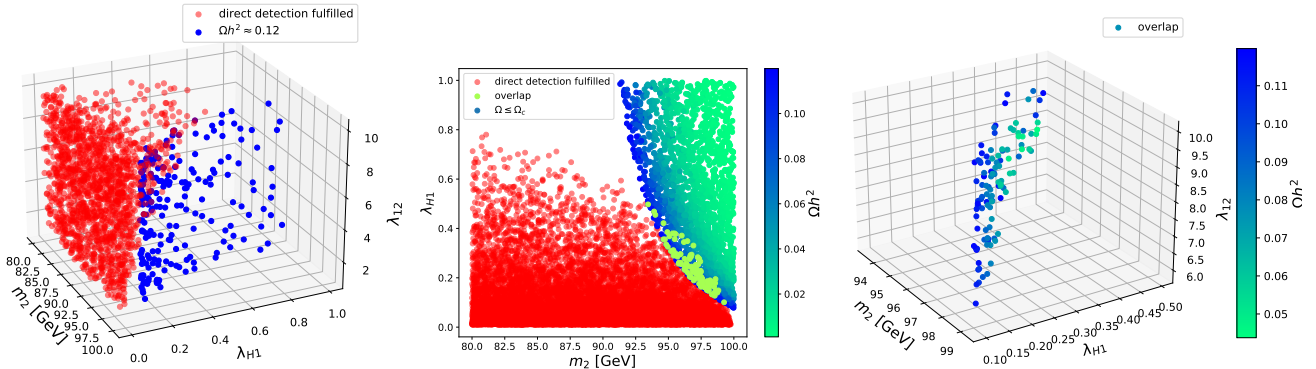


Figure 5: Random scan on the inverted mass hierarchy ($m_2 < m_1$) parameter space for fixed $m_1 = 100$ GeV and $\lambda_{H2} = 0$. The red points fulfill the direct detection constraints, while the blue-green points fulfill $\Omega \leq \Omega_c$ (with Ω indicated by the color bar). The left plot shows points projected on the 3d parameter space ($m_1, \lambda_{H1}, \lambda_{12}$), the middle plot shows the projection on the plane $m_1 - \lambda_{H1}$ plane, and the right plot shows just the overlap of points fulfilling the direct detection constraints and the relaxed abundance constraint $\Omega \leq \Omega_c$.

at very small couplings λ_{H1} and arbitrary λ_{12} , or, for larger couplings λ_{H1} and λ_{12} at masses m_2 mostly below that fulfilling the abundance constraint for the given couplings. Since in the inverted mass hierarchy a lower relic abundance at equal couplings can only be achieved by a smaller mass difference, points fulfilling $\Omega < \Omega_c$ lie opposite from the points fulfilling the direct detection constraints, with the points fulfilling $\Omega = \Omega_c$ forming a boundary. Hence the overlap of these two regions does not increase significantly when relaxing the abundance constraint. This fact is shown in Fig. 5 (middle) where the small overlap of points fulfilling the direct detection and relaxed abundance constraint is shown. In particular from Fig. 5 (right) we see no overlap for $\lambda_{12} \lesssim 6$, since smaller λ_{12} also requires small λ_{H1} to pass the direct detection constraint which in turn produces a DM over-abundance.

To get a more precise picture of the interplay between the parameter space allowed by the experimental and the theoretical constraints, in Fig. 6 we show a plot of the allowed points with $m_1 = 100$ and 500 GeV projected in the plane $(\lambda_{H1}, \lambda_{12})$, with a color bar for m_2 . The left plot shows the same parameter space as Fig. 5, and confirms that sizable values for λ_{12} are required in order to fulfill the experimental DM constraints. Further, as shown in the right plot, for a higher m_1 , the smallest possible values for λ_{12} increase as well. Interestingly, the smallest achievable λ_{12} couplings in each case are around 6 and 8 (left/right plots), and they are achieved for very particular mass splittings, 1 GeV in the left case and around 5 GeV in the right plot. As suggested by Fig. 6, with growing m_1 , the allowed parameter space shrinks. We have checked numerically that the minimum allowed λ_{12} by direct detection and relic abundance constraints in the range for m_1 from $m_h/2$ up to 1 TeV does not change by more than a factor of two.

As was argued in Section 2, it is necessary that the coupling values be in agreement with

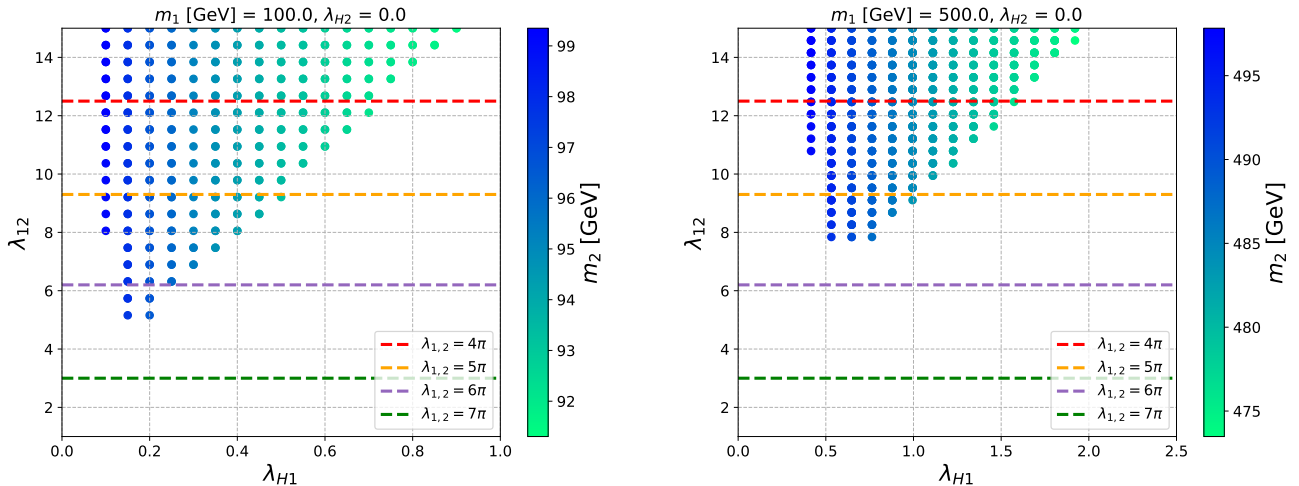


Figure 6: Allowed points by experimental constraints considering $m_1 = 100$ GeV (left) and 500 GeV (right) projected in the plane $(\lambda_{H1}, \lambda_{12})$. The color bar indicates the mass of S_2 . The dashed lines correspond to the maximum value allowed for λ_{12} considering that the theoretical constraints allowed quartic couplings up to the corresponding value indicated on the legend.

perturbativity and unitarity, which depend on the values of the quartic couplings. In the Fig. 6 we show the contours of the unitarity constraints for different $\lambda_{1,2}$. The points below each dashed line are allowed by unitarity for a certain range of values of $\lambda_{1,2}$. For instance, all the points below the yellow dashed line are allowed for $\lambda_{1,2}$ up to 5π . If the values of $\lambda_{1,2}$ are below 4π , then the corresponding unitarity dashed line rises above the red dashed line, and the allowed parameter space will depend only on the perturbative limit assumed on $\lambda_{H1}, \lambda_{12}$. As a complementary analysis, in Appx. B we discuss the effects of the radiative generation of λ_{H2} on the results shown in Fig. 6.

4.3 Landau Poles

As a result of the previous section, high coupling values are necessary to obtain the correct relic abundance evading direct detection bounds, especially for λ_{12} . However, in a scalar theory like this one, such large couplings grow rapidly with the energy scale according to the one-loop renormalization group equations (RGE). Estimating to what extent this model will be valid in the high energy regime, i.e. before some of the couplings reach a *Landau pole*, is therefore vital for its application. The criteria used here to find the Landau poles is simply one of the couplings exceeding 4π according to RGE evolution. In the following, we will study the energy validity of the model in a general way, then for simplicity assuming λ_1 and λ_2 negligible.

Apart of the existing β functions for the SM couplings, from the two DM scalar model we

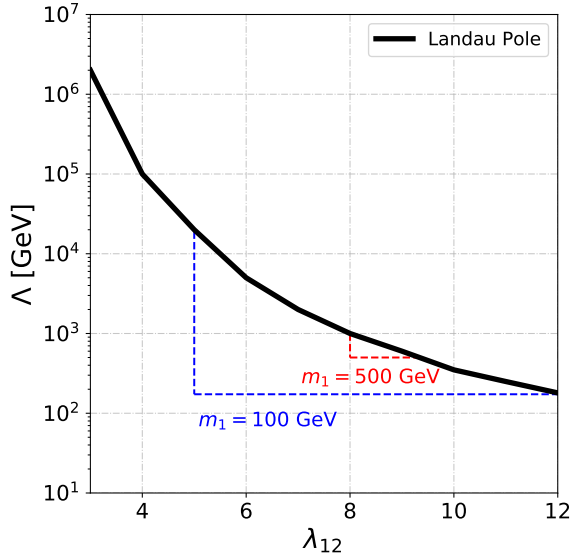


Figure 7: Energy scale at which a Landau pole appears in the two-scalar DM assisted freeze-out framework as a function of $\lambda_{12}(m_t)$, considering $\lambda_{H1}(m_t) = 0.1, 0.5, 1.0$ and 1.5 . The regions enclosed by the dashed curves are allowed considering $m_1 = 100$ GeV (blue) and $m_2 = 500$ GeV (red).

obtain [15]

$$\begin{aligned}
16\pi^2\beta_{\lambda_H} &= \frac{3}{8}g_1^4 + \frac{9}{8}g_2^4 + \frac{3}{4}g_1^2g_2^2 - 6y_t^4 + 24\lambda_H^2 + 12y_t^2\lambda_H - 3g_1^2\lambda_H - 9g_2^2\lambda_H + \frac{1}{2}(\lambda_{H1}^2 + \lambda_{H2}^2), \\
16\pi^2\beta_{\lambda_{H1}} &= \lambda_{H1} \left(12\lambda_H + \lambda_{12} + 4\lambda_{H1} + 6y_t^2 - \frac{3}{2}g_1^2 - \frac{9}{2}g_2^2 \right) + \lambda_{H2}\lambda_{12}, \\
16\pi^2\beta_{\lambda_{H2}} &= \lambda_{H2} \left(12\lambda_H + \lambda_{12} + 4\lambda_{H2} + 6y_t^2 - \frac{3}{2}g_1^2 - \frac{9}{2}g_2^2 \right) + \lambda_{H1}\lambda_{12}, \\
16\pi^2\beta_{\lambda_{12}} &= 4\lambda_{12}^2 + 4\lambda_{H1}\lambda_{H2},
\end{aligned} \tag{21}$$

where $\beta_\lambda \equiv \mu \frac{d\lambda}{d\mu}$, with μ the renormalization scale, g_1, g_2, g_3 are the gauge couplings for $U(1), SU(2), SU(3)$, respectively, and y_t is the top quark Yukawa coupling. We solve this system using *RGE package*⁶, considering the following initial conditions evaluated at $\mu = m_t = 173$ GeV: $g_1(m_t) = \sqrt{5/3} \times 0.359, g_2(m_t) = 0.647, g_3(m_t) = 1.166, y_t(m_t) = 0.950, \lambda_H(m_t) = 0.128, \lambda_{H2}(m_t) = 0$, whereas the values for $\lambda_{H1}(m_t)$ and $\lambda_{12}(m_t)$ are specified in the following discussion. As the last line in eq. (4.3) shows $\beta_{\lambda_{12}} \propto \lambda_{12}^2$ and the values obtained in the previous section resulted to be $\lambda_{12}(m_t) \gtrsim 5$, a strongly growing behavior with energy is expected for λ_{12} , resulting in Landau poles at relatively low energy scales. In Fig. 7 we show how the maximum energy Λ at which the coupling λ_{12} reaches its Landau pole (black solid

⁶RGERun 2: Solving Renormalization Group Equations in Effective Field Theories (K. Kannike).

line) decreases as $\lambda_{12}(m_t)$ becomes bigger. Variations of $\lambda_{H1}(m_t)$ in the range $0.1 - 1.5$ do not give rise to significant deviations respect to the black curve. Additionally, the parameter space found in the last section for $m_1 = 100$ and 500 GeV is reflected as the regions inside the dashed and continuous curves. That is, for $m_1 = 100$ GeV, the blue vertical dashed line is the minimum value found for λ_{12} , whereas the horizontal line is the initial renormalization scale $\mu = m_t$. As λ_{12} at the EW scale gets larger, the validity of the model becomes greatly constrained at high energies, showing a Landau pole already at a few hundred GeV. For higher masses, the situation becomes even more drastic, as shown for $m_1 = 500$ GeV with the red dashed lines, where $\lambda_{12} \gtrsim 9$ reaches a Landau pole below the masses of the singlet scalars.

Therefore, it is clear that high coupling values at the EW scale set limitations for the model at high energies, especially if we want to study the two-DM scalars in the assisted freeze-out in a cosmological context (e.g. [37]). Possible extensions to this scenario can be thought of in order to evade such large couplings. For instance, adding to the present model a vector-like lepton which transform non-trivially under one of the discrete symmetries opens up a new annihilation channel for $S_1 S_1$ annihilations, reducing significantly the high values for λ_{12} required in the present work [38].

5 Discussion and Summary

In this paper we investigated to what extent the parameter space of the Singlet Higgs Portal can be reopened by introducing a second DM candidate decoupled from the SM: *Assisted freeze-out framework*. The outcome is positive.

We conclude that, in order to evade direct detection and relic abundance constraints outside the Higgs resonance region it is required that one of the key new parameters λ_{12} takes high values, which are constrained by theoretical considerations of the potential stability, perturbativity and unitarity. In this way small regions in the parameter space reopen for DM masses around a few hundred GeV. Additionally, our results are in accordance with what was found [11], where the authors studied a model in an similar framework. In the present work, we explored in major detail the parameter space, concluding that outside the resonance region, DM can be explained in the two scalar model if $m_{decoupled} < m_{coupled}$ with a relative mass difference of up to roughly 10% in the most optimistic cases (i.e. if we allow a very large coupling λ_{12}).

Similarly to the SHP, the two real scalar model in the assisted freeze-out regime shows that parts of the Higgs resonance region remain not (yet) ruled out by experimental data. In fact, due to the additional degrees of freedom m_2 and λ_{12} , the two scalar model in the assisted freeze-out framework could completely explain DM for a broader range of values m_1 and λ_{H1} , however, the explanation would still require m_1 in the region of $m_h/2$ and simultaneously a very small mass splitting between m_1 and m_2 .

Finally, we have shown that one-loop RGE imply that the high couplings at the EW scale found in this work, i.e. $\lambda_{12} \sim \mathcal{O}(5 - 10)$, imply a very low energy validity for the model with two stable scalars, requiring a UV completion at low energy scales for the model to be viable at

higher energies. Alternatives have been proposed too, such as to include a vector-like fermion portal at the EW scale.

6 Acknowledgment

B.D.S. would like to thank Roger Galindo, Felipe Rojas, Sebastian Norero and Gorazd Cvetič for useful discussions, and to CONICYT Grant No. 74200120.

A Average Annihilation Cross Sections

For a scattering process $ij \rightarrow ab$, the average cross section times velocity following a Maxwell-Boltzmann thermal distribution is given by

$$\langle \sigma_{ijab} v \rangle = \frac{1}{n_{ie} n_{ie}} \int \frac{d^3 p_i}{(2\pi)^3} \int \frac{d^3 p_j}{(2\pi)^3} (\sigma_{ijab} v) \cdot e^{-(E_i + E_j)/T}, \quad (22)$$

where v denotes the Møller velocity, and n_{ie} the equilibrium densities given in eq. (12). The cross sections for the processes we are going to consider can be written as functions of $s := (E_i + E_j)^2 - (\vec{p}_i + \vec{p}_j)^2$. The integrals in eq. (22) then break down to just a single integral over s

$$\langle \sigma v \rangle = \int_{(m_i + m_j)^2}^{\infty} ds \frac{(\sigma v)^{(cm)} \cdot s \cdot K_1(\frac{\sqrt{s}}{T})}{16T m_i^2 m_j^2 K_2(\frac{m_i}{T}) K_2(\frac{m_j}{T})} \sqrt{\frac{(m_i^2 - m_j^2)^2}{s} + s - 2(m_i^2 + m_j^2)}, \quad (23)$$

where $(\sigma v)^{(cm)}$ denotes the calculation in the center of mass frame and K_α is the modified Bessel function of the second kind. Similarly, $\langle s \rangle$ (for $m_i = m_j$) can now be calculated in reverse. Since $s = 4m_i^2 + 4p_{(cm)}^2$, then

$$\langle s \rangle = \frac{1}{n_{ie}} \int \frac{d^3 p}{(2\pi)^3} (4m_i^2 + 4p^2) e^{-E/T} = 4m_i^2 + 12m_i T K_3(\frac{m_i}{T}) / K_2(\frac{m_i}{T}). \quad (24)$$

Away from resonances for large x , the averaged annihilation cross section is then approximately

$$\langle \sigma v \rangle \approx \sigma v(\langle s \rangle) \approx \sigma v \left(4m_i^2 \left(1 + \frac{3}{x} \frac{\mu}{m_i} \right) \right) \approx \sigma v(4m_i^2) \quad (25)$$

Near the Higgs resonance, i.e. $m_1 \lesssim m_h/2$, we used the well known approximation for σv in eq. (23), which replaced the propagator by a Dirac delta function (Narrow Width Approximation):

$$\frac{1}{(s - m_h^2)^2 + m_h^2 \Gamma^2} \approx \frac{\pi}{m_h \Gamma} \delta(s - m_h^2), \quad (26)$$

where Γ is the total Higgs decay width, including the invisible decays into DM particles. Using this approximation, the integral in eq. (23) becomes an algebraic expression. In Fig. 8 we compare the approximations to the result from `micrOMEGAs` in the region (i) below and (ii) above the Higgs resonance. Considering two temperatures, $x = 5$ and 20, we show that our approximation (red solid curve) matches very well the `micrOMEGAs` result in the resonance region (i).

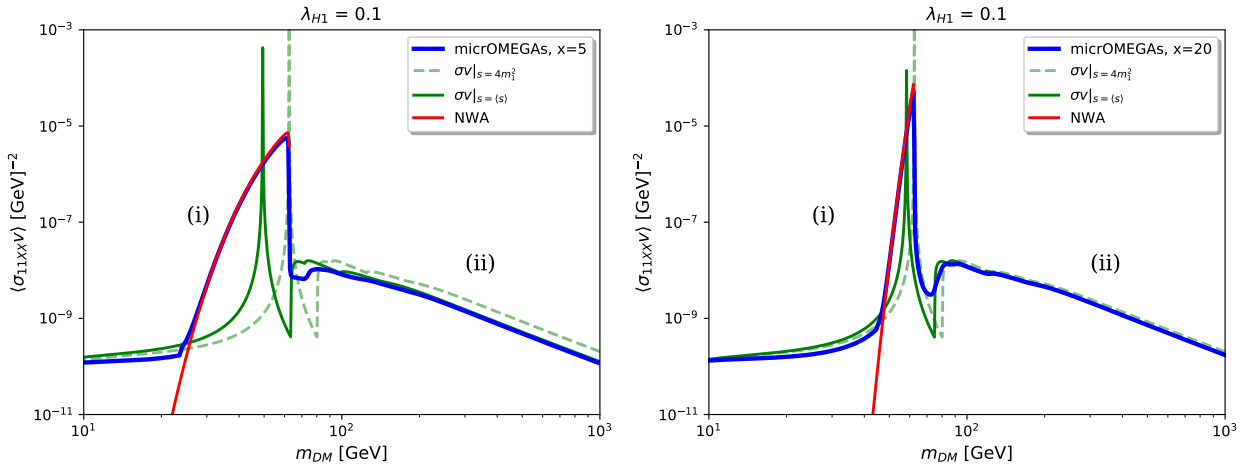


Figure 8: Comparison of $\langle\sigma_{11XX}v\rangle$ as a function of m_1 calculated using the NWA (red) and the constant approximation with (green) and without the $\frac{3}{x}$ correction (green dashed). We set $\lambda_{H1} = 0.1$ and $x = 5$ (left), respectively $x = 20$ (right). For comparison we also plotted the result obtained with `micrOMEGAs` (blue solid line).

B $S_2 S_2 h$ vertex at one-loop

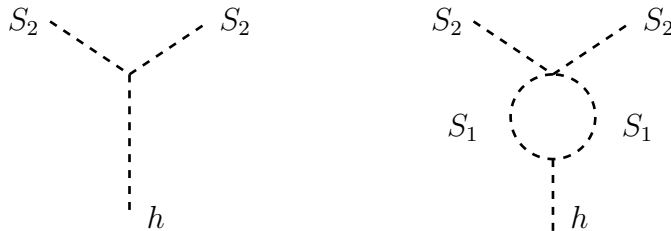


Figure 9: Tree-level $S_2 S_2 h$ vertex and the main one-loop corrections in the two real scalar model with $Z_2 \times Z'_2$ symmetry in the limit $\lambda_{H2} \ll 1$.

In this appendix we show the calculation of the one-loop λ_{H2} coupling and its effects on the relic abundances of S_1 and S_2 . As we are assuming that at tree level $\lambda_{H2} \ll (\lambda_{H1}, \lambda_{12})$, the

only diagram which contributes to the vertex S_2S_2h at one-loop is given in the right side of Fig. 9, whose amplitude is given by

$$\Gamma^{1\text{-loop}}(p^2) = (-i\lambda_{12})(-i\lambda_{H1}v_H)\frac{1}{2}\int\frac{d^4p_1}{(2\pi)^4}\frac{i}{(p_1-p)^2-m_1^2}\frac{i}{p_1^2-m_1^2}, \quad (27)$$

where $p_1+p_2=p$ and the $1/2$ is a symmetry factor due to the scalar loop. After some manipulation via Feynman parameters, and using dimensional regularization, we have

$$\Gamma^{1\text{-loop}}(p^2) = \frac{1}{16\pi^2}\lambda_{12}\lambda_{H1}B_0(p^2, m_1^2, m_1^2), \quad (28)$$

where $B_0(p^2, m_1^2, m_1^2) = 2/\epsilon + \mathcal{B}(p^2, m_1^2, m_1^2)$, with

$$\mathcal{B}(p^2, m_1^2, m_1^2) = -\log\frac{m_1^2}{\tilde{\mu}^2} - \int_0^1 dx \log\left[1-x(1-x)\frac{p^2}{m_1^2}\right] \quad (29)$$

where $\tilde{\mu}^2 = 4\pi e^{-\gamma_E}\mu^2$ is a mass dimension parameter introduced to keep coupling constants dimensionless in d -dimensions.

The renormalized (finite) amplitude is given by

$$\begin{aligned} \Gamma(p^2) &= \Gamma^{\text{tree}} + \Gamma^{1\text{-loop}} + \Gamma^{\text{counter}}. \\ &= \lambda_{H2}v_H + \frac{1}{16\pi^2}\lambda_{12}\lambda_{H1}v_H B_0(p^2, m_1^2, m_1^2) + \delta_2\lambda_{H2}v_H \end{aligned} \quad (30)$$

where δ_2 corresponds to the counter-term which is going to cancel the divergence from the second term in the right side of eq. (30). After imposing the renormalization condition $\Gamma(p_0^2) = \lambda_{H2}v_H$, with p_0^2 some low energy scale, the amplitude becomes:

$$\Gamma(p^2) = \lambda_{H2}v_H + \frac{1}{16\pi^2}\lambda_{12}\lambda_{H1}v_H \int_0^1 dx \log\left[\frac{1-x(1-x)\frac{p_0^2}{m_1^2}}{1-x(1-x)\frac{p^2}{m_1^2}}\right] \quad (31)$$

Taking that the renormalization scale very low (i.e. $p_0^2 \ll (m_1^2, m_2^2)$), and considering that at freeze-out we have that $p^2 \approx 4m_2^2$, then eq. (31) becomes

$$\Gamma_{S_2S_2h} \approx \left(\lambda_{H2} + \frac{\lambda_{12}\lambda_{H1}}{16\pi^2}\right)v_H. \quad (32)$$

for $m_2 \lesssim m_1$, in agreement with [8]. Additionally, the loop contribution has a completely negligible effect for direct detection such as XENON1T, due to the low transfer momentum $|p| \sim \mathcal{O}(\text{keV})$.

In Fig. 10 we show the changes in the relic abundances as a function of λ_{H2} , considering some points of Fig. 6 with the correct relic abundance and evading direct detection. The vertical

lines represent the one-loop value of λ_{H2} ($= \lambda_{H1}\lambda_{12}/16\pi^2$) for the chosen points indicated in the plot. In both plots, the highest combination of values of $\lambda_{H1}\lambda_{12}$ (grey dashed lines) deviate the relic abundances predictions in a factor of two with respect to the simplest case in which $\lambda_{H2} = 0$. Note that these high coupling values must to be in agreement with the chosen perturbative/unitarity criteria. As it is shown in Fig. 6, the values for the pair $(\lambda_{H1}, \lambda_{12})$ given by the dashed vertical lines in both plots of Fig. 10 are valid provided that $(\lambda_1, \lambda_2) \leq 4\pi$. Oppositely, higher values for (λ_1, λ_2) implies lower values for the pair $(\lambda_{H1}, \lambda_{12})$, then the effect of the radiative coupling λ_{H2} becomes weaker. Finally, we have checked that these typical radiative values for λ_{H2} shown in Fig. 10 do not change our conclusions in Sec. 2.

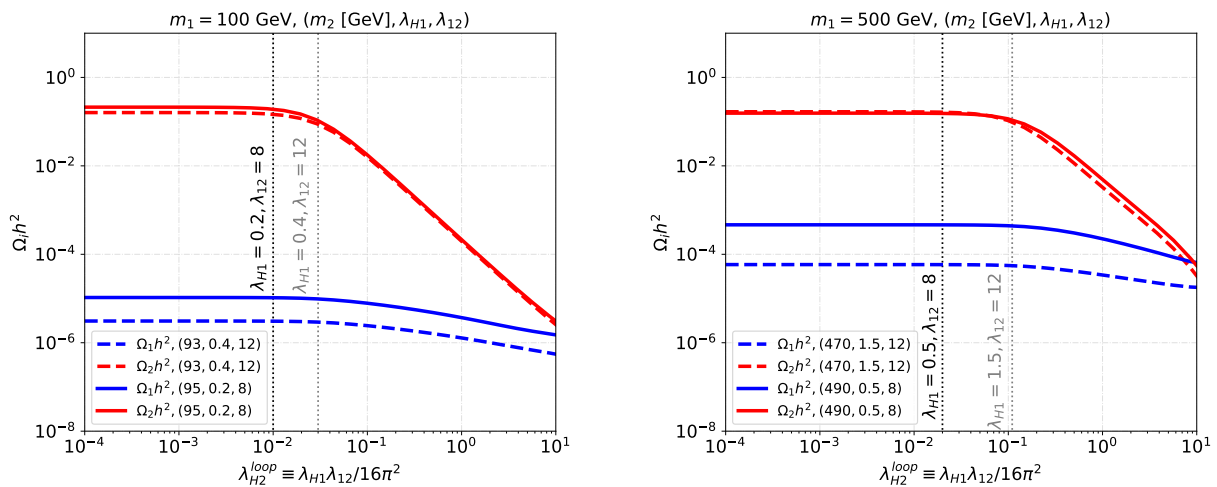


Figure 10: Relic abundances as a function of $\lambda_{H2} \equiv \lambda_{H1}\lambda_{12}/16\pi^2$, for $m_1 = 100$ GeV (left) and $m_1 = 500$ GeV (right), with the rest of the parameters specified in the plots.

References

- [1] Planck collaboration, N. Aghanim et al., “Planck 2018 results. VI. Cosmological parameters,” (2018), [arXiv:1807.06209 \[astro-ph.CO\]](#).
- [2] J. M. Cline, K. Kainulainen, P. Scott, and C. Weniger, “Update on scalar singlet dark matter,” *Phys. Rev. D* **88** (2013) 055025, [arXiv:1306.4710 \[hep-ph\]](#). [Erratum: *Phys.Rev.D* 92, 039906 (2015)].
- [3] **GAMBIT** Collaboration, P. Athron *et al.*, “Status of the scalar singlet dark matter model,” *Eur. Phys. J. C* **77** no. 8, (2017) 568, [arXiv:1705.07931 \[hep-ph\]](#).
- [4] B. Dasgupta, E. Ma, and K. Tsumura, “Weakly interacting massive particle dark matter and radiative neutrino mass from Peccei-Quinn symmetry,” *Phys. Rev. D* **89** no. 4, (2014) 041702, [arXiv:1308.4138 \[hep-ph\]](#).

- [5] A. Abada, D. Ghaffor, and S. Nasri, “A Two-Singlet Model for Light Cold Dark Matter,” *Phys. Rev.* **D83** (2011) 095021, [arXiv:1101.0365 \[hep-ph\]](#).
- [6] A. Ahriche, A. Arhrib, and S. Nasri, “Higgs Phenomenology in the Two-Singlet Model,” *JHEP* **02** (2014) 042, [arXiv:1309.5615 \[hep-ph\]](#).
- [7] K. Ghorbani and H. Ghorbani, “Scalar split WIMPs in future direct detection experiments,” *Phys. Rev. D* **93** no. 5, (2016) 055012, [arXiv:1501.00206 \[hep-ph\]](#).
- [8] J. A. Casas, D. G. Cerdeño, J. M. Moreno, and J. Quilis, “Reopening the Higgs portal for single scalar dark matter,” *JHEP* **05** (2017) 036, [arXiv:1701.08134 \[hep-ph\]](#).
- [9] V. R. Shajiee and A. Tofghi, “Electroweak Phase Transition, Gravitational Waves and Dark Matter in Two Scalar Singlet Extension of The Standard Model,” *Eur. Phys. J. C* **79** no. 4, (2019) 360, [arXiv:1811.09807 \[hep-ph\]](#).
- [10] A. Arhrib and M. Maniatis, “The two-real-singlet Dark Matter model,” *Physics Letters B* **796** (2019) 15 – 19, [arXiv:1807.03554 \[hep-ph\]](#).
- [11] T. N. Maity and T. S. Ray, “Exchange driven freeze out of dark matter,” *Phys. Rev. D* **101** no. 10, (2020) 103013, [arXiv:1908.10343 \[hep-ph\]](#).
- [12] M. Maniatis, “Light dark matter in a minimal extension with two additional real singlets,” *Phys. Rev. D* **103** no. 1, (2021) 015010, [arXiv:2005.13443 \[hep-ph\]](#).
- [13] G. Belanger and J.-C. Park, “Assisted freeze-out,” *JCAP* **1203** (2012) 038, [arXiv:1112.4491 \[hep-ph\]](#).
- [14] F. Bazzocchi and M. Fabbrichesi, “A simple inert model solves the little hierarchy problem and provides a dark matter candidate,” *Eur. Phys. J. C* **73** no. 2, (2013) 2303, [arXiv:1207.0951 \[hep-ph\]](#).
- [15] K. P. Modak, D. Majumdar, and S. Rakshit, “A Possible Explanation of Low Energy γ -ray Excess from Galactic Centre and Fermi Bubble by a Dark Matter Model with Two Real Scalars,” *JCAP* **03** (2015) 011, [arXiv:1312.7488 \[hep-ph\]](#).
- [16] K. Ghorbani and H. Ghorbani, “Scalar Dark Matter in Scale Invariant Standard Model,” *JHEP* **04** (2016) 024, [arXiv:1511.08432 \[hep-ph\]](#).
- [17] S. Bhattacharya, P. Poullose, and P. Ghosh, “Multipartite Interacting Scalar Dark Matter in the light of updated LUX data,” *JCAP* **04** (2017) 043, [arXiv:1607.08461 \[hep-ph\]](#).
- [18] M. Pandey, D. Majumdar, and K. P. Modak, “Two Component Feebly Interacting Massive Particle (FIMP) Dark Matter,” *JCAP* **06** (2018) 023, [arXiv:1709.05955 \[hep-ph\]](#).

- [19] K. Ghorbani and P. H. Ghorbani, “A Simultaneous Study of Dark Matter and Phase Transition: Two-Scalar Scenario,” *JHEP* **12** (2019) 077, [arXiv:1906.01823 \[hep-ph\]](#).
- [20] L. Bian, R. Ding, and B. Zhu, “Two Component Higgs-Portal Dark Matter,” *Phys. Lett. B* **728** (2014) 105–113, [arXiv:1308.3851 \[hep-ph\]](#).
- [21] S. Bhattacharya, A. Drozd, B. Grzadkowski, and J. Wudka, “Two-Component Dark Matter,” *JHEP* **10** (2013) 158, [arXiv:1309.2986 \[hep-ph\]](#).
- [22] K. Agashe, Y. Cui, L. Necib, and J. Thaler, “(In)direct Detection of Boosted Dark Matter,” *JCAP* **10** (2014) 062, [arXiv:1405.7370 \[hep-ph\]](#).
- [23] G. Arcadi, C. Gross, O. Lebedev, S. Pokorski, and T. Toma, “Evading Direct Dark Matter Detection in Higgs Portal Models,” *Phys. Lett. B* **769** (2017) 129–133, [arXiv:1611.09675 \[hep-ph\]](#).
- [24] B. Díaz Sáez, P. Escalona, S. Norero, and A. Zerwekh, “Fermion Singlet Dark Matter in a Pseudoscalar Dark Matter Portal,” [arXiv:2105.04255 \[hep-ph\]](#).
- [25] Q.-H. Cao, E. Ma, J. Wudka, and C. P. Yuan, “Multipartite dark matter,” [arXiv:0711.3881 \[hep-ph\]](#).
- [26] K. Kannike, “Vacuum Stability Conditions From Copositivity Criteria,” *Eur. Phys. J. C* **72** (2012) 2093, [arXiv:1205.3781 \[hep-ph\]](#).
- [27] K. Kannike, “Vacuum Stability of a General Scalar Potential of a Few Fields,” *Eur. Phys. J. C* **76** no. 6, (2016) 324, [arXiv:1603.02680 \[hep-ph\]](#). [Erratum: *Eur.Phys.J.C* **78**, 355 (2018)].
- [28] P. M. Ferreira, “The vacuum structure of the Higgs complex singlet-doublet model,” *Phys. Rev. D* **94** no. 9, (2016) 096011, [arXiv:1607.06101 \[hep-ph\]](#).
- [29] B. W. Lee, C. Quigg, and H. B. Thacker, “Weak Interactions at Very High-Energies: The Role of the Higgs Boson Mass,” *Phys. Rev. D* **16** (1977) 1519.
- [30] G. Cynolter, E. Lendvai, and G. Pocsik, “Note on unitarity constraints in a model for a singlet scalar dark matter candidate,” *Acta Phys. Polon. B* **36** (2005) 827–832, [arXiv:hep-ph/0410102](#).
- [31] L. Husdal, “On Effective Degrees of Freedom in the Early Universe,” *Galaxies* **4** no. 4, (2016) 78, [arXiv:1609.04979 \[astro-ph.CO\]](#).
- [32] T. Binder, T. Bringmann, M. Gustafsson, and A. Hryczuk, “Early kinetic decoupling of dark matter: when the standard way of calculating the thermal relic density fails,” *Phys. Rev. D* **96** no. 11, (2017) 115010, [arXiv:1706.07433 \[astro-ph.CO\]](#). [Erratum: *Phys.Rev.D* **101**, 099901 (2020)].

- [33] P. Gondolo and G. Gelmini, “Cosmic abundances of stable particles: Improved analysis,” *Nucl. Phys. B* **360** (1991) 145–179.
- [34] J. L. Feng and J. Smolinsky, “Impact of a resonance on thermal targets for invisible dark photon searches,” *Phys. Rev. D* **96** no. 9, (2017) 095022, [arXiv:1707.03835](https://arxiv.org/abs/1707.03835) [hep-ph].
- [35] J. e. a. Aprile, E. Aalbers, “Dark matter search results from a one ton-year exposure of xenon1t,” *Physical Review Letters* **121** no. 11, (Sep, 2018) .
<http://dx.doi.org/10.1103/PhysRevLett.121.111302>.
- [36] **CMS** Collaboration, A. M. Sirunyan *et al.*, “Search for invisible decays of a Higgs boson produced through vector boson fusion in proton-proton collisions at $\sqrt{s} = 13$ TeV,” *Phys. Lett. B* **793** (2019) 520–551, [arXiv:1809.05937](https://arxiv.org/abs/1809.05937) [hep-ex].
- [37] R. N. Lerner and J. McDonald, “Gauge singlet scalar as inflaton and thermal relic dark matter,” *Phys. Rev. D* **80** (2009) 123507, [arXiv:0909.0520](https://arxiv.org/abs/0909.0520) [hep-ph].
- [38] B. D. Sáez and K. Ghorbani, “Singlet Scalars as Dark Matter and the Muon g-2 Anomaly,” [arXiv:2107.08945](https://arxiv.org/abs/2107.08945) [hep-ph].